Eur. Phys. J. C (2025) 85:633
https://doi.org/10.1140/epjc/s10052-025-14280-0

THE EUROPEAN PHYSICAL JOURNAL C

Regular Article - Theoretical Physics

Testing of QPOs, particle dynamics, emission energy and thermal fluctuation around a regular hairy black hole

Asifa Ashraf[1,a], **Allah Ditta**[3,b], **Tayyab Naseer**[4,c], **S. K. Maurya**[5,2,d], **Saibal Ray**[6,e], **Phongpichit Channuie**[8,7,f], **Farruh Atamurotov**[9,10,g]

[1] School of Mathematical Sciences, Zhejiang Normal University, Jinhua 321004, Zhejiang, China
[2] Research Center of Astrophysics and Cosmology, Khazar University, 41 Mehseti Street, AZ1096 Baku, Azerbaijan
[3] Department of Mathematics, School of Science, University of Management and Technology, Lahore 54000, Pakistan
[4] Department of Mathematics and Statistics, The University of Lahore, 1-KM Defence Road, Lahore 54000, Pakistan
[5] Department of Mathematical and Physical Sciences, College of Arts and Sciences, University of Nizwa, Nizwa 616, Sultanate of Oman
[6] Centre for Cosmology, Astrophysics and Space Science (CCASS), GLA University, Mathura, Uttar Pradesh 281406, India
[7] School of Science, Walailak University, Nakhon Si Thammarat 80160, Thailand
[8] College of Graduate Studies, Walailak University, Nakhon Si Thammarat 80160, Thailand
[9] New Uzbekistan University, Movarounnahr street 1, Tashkent 100000, Uzbekistan
[10] Urgench State University, Kh. Alimdjan Str. 14, Urgench 220100, Uzbekistan

Received: 16 December 2024 / Accepted: 4 May 2025

Abstract We investigate the dynamics of test particles around a spherically symmetric, non-rotating, hairy regular black hole, examining how the model parameters affect particle motion. The black hole is characterized by two parameters, the mass M and a hairy parameter α. Using the effective potential, we examine the stability of circular orbits. We derive analytical expressions for the energy and angular momentum of test particles as a function of the black hole parameters. The effective forces acting on particles and the innermost stable circular orbits are also examined. Additionally, we numerically integrate the equations of motion to examine particle trajectories and further investigate their motion. Epicyclic oscillations of test particles close to the equatorial plane are explored, and analytical expressions for radial, vertical, and orbital frequencies are derived as functions of the black hole parameters. We also examine the frequency of periastron precession of the particles. We compare the motion of test particles around a hairy regular black hole with the particle motion around a classical non-rotating Schwarzschild black hole. Further, we discuss thermally fluctuating phenomena by using the Tsallis entropy and the energy emission process. Our findings show that the black hole model's parameters significantly impact particle motion and thermal features.

1 Introduction

Black holes (BHs) are some of the most compelling and enigmatic subjects of study in contemporary physics because of their unique properties and structural complexities. Their visible exposures serve as significant indicators to unravel the puzzles associated with these celestial objects. A monumental achievement in this regard took place in 2019 when the Event Horizon Telescope (EHT) Collaboration captured the first-ever image of the accretion flow enclosed by a supermassive BH lying at the center of the *M87** galaxy [1,2]. This marked a crucial moment for researchers seeking to explore the properties of BHs by enabling validation of their work with observations [3]. Subsequent to this, in 2022, the same collaboration disclosed an image of *Sgr A**, a supermassive BH located at the center of our galaxy, which further advances our understanding of these giants [4–6]. The EHT aimed to explore supermassive BHs that are located at the centers of galaxies. Collecting data from multiple radio telescopes that are located throughout the world helps in accomplishing this objective. Through collective functioning, a virtual instru-

[a] e-mail: asifamustafa3828@gmail.com
[b] e-mail: mradshahid01@gmail.com
[c] e-mails: tayyab.naseer@math.uol.edu.pk; tayyabnaseer48@yahoo.com
[d] e-mail: sunil@unizwa.edu.om
[e] e-mail: saibal.ray@gla.ac.in
[f] e-mail: phongpichit.ch@mail.wu.ac.th (corresponding author)
[g] e-mail: atamurotov@yahoo.com

Published online: 10 June 2025

ment is created by these telescopes with an efficient fissure in comparison with the Earth's diameter. The angular resolution has been considerably improved by such a configuration, allowing one to observe massive structures at a scale equivalent to the event horizon of a BH.

An intriguing element regarding the dynamics of the test particles surrounding BHs is its link with the quasiperiodic oscillations (QPOs) that are observed during the X-ray emissions of certain micro-quasars [7]. Therefore, it is worthwhile to examine QPOs from an astrophysical perspective, as it provides considerable support for the credibility of gravitational models functioning under sufficiently strong field conditions. Furthermore, QPOs serve as effective indications for determining the spin and other properties of BHs [8,9]. In the field of research related to astrophysics, these oscillations have served an essential purpose since their identification nearly 30 years ago. A class of theoretical frameworks have been proposed to explain their origins, including (i) warped disk, (ii) disk-seismic, (iii) resonance, and (iv) hot-spot models [10]. The precise physical nature behind the origin of QPOs still remains unclear. They continue to be an appealing subject of study within the context of Einstein's relativity and other modified theories [11–18]. For those interested in studying the physical origins and observational attributes of QPOs, more information can be found in [19]. Several interesting works are available in the literature that discuss various aspects of multiple BH geometries [20–28]. Interesting work on QPOs has recently been reported in [29–37].

Studying the extraordinary conditions surrounding BHs provides an opportunity to explore the motion of particles in these regions. Such regions around a BH often provide a platform to test predictions made in Einstein's theory of relativity. It is obvious that the moving particles' paths and trajectories of light and matter existing near a BH's event horizon are profoundly influenced. The particles that exist near a BH may significantly alter their behavior on the basis of the attributes of the BH (for instance, its mass, spin, and charge). As a result, one can gain valuable insights into the properties of spacetime near a BH by analyzing these paths. Importantly, it has been revealed through governing equations of motion that when a particle approaches the event horizon, it experiences considerable relativistic phenomena such as gravitational redshift and time dilation. Both phenomena are notable at the nearest point on which a moving particle can have an orbit around a BH without succumbing to the pull of gravity [38]. Moreover, the results obtained from these explorations have considerable implications for identifying gravitational waves. The dynamics of the moving particles in a sufficiently strong gravitational field play a critical role when discussing the merger and spiral phases [39–45].

Another pivotal notion in BH physics is the no-hair theorem, which has a major role in the study of such celestial bodies. According to this theorem, we can characterize a BH by only three of its observable parameters, namely mass, electric charge (if charge is present in the BH under consideration), and angular momentum. The analogy of "without hair" suggests that BHs lack discriminating properties or "hair" that would help reveal data or information on the matter used in their formation or that falls into them. At the moment when a BH achieves its stable state, all information related to its creation and the matter that was used in its formation becomes unattainable to external observers, as it remains bound within the event horizon [46]. This leads to important implications for us in broadening our understanding regarding preservation of the information in the universe and raises penetrating questions about what the "reality" is, as explained by general relativity versus quantum mechanics. The photon ring, illuminated by the accretion disk within a strong gravitational field, serves as a crucial tool for identifying the shadow of a BH [47]. However, the no-hair theorem has shown potential exceptions in certain scenarios [48,49]. Recent discoveries of "hairy" BH solutions—those that require additional parameters beyond conserved charges—have opened new avenues for investigating possible violations of the no-hair theorem. Notable examples of these solutions include various models that challenge traditional understandings of BH characteristics [50–54].

Research into periodic orbits is crucial for unraveling the fundamental characteristics of BHs, as these orbits can reveal insights into their formation mechanisms and the dynamics of particles in their vicinity. Levin and colleagues [55] introduced a systematic classification for periodic orbits, represented by three integers, w, z, and v, which correspond to the rotation, scaling, and vertex behavior of the orbit, respectively. This leads to the definition of the quantity $q = \frac{w+v}{z}$. When q is irrational, the orbit exhibits a precessing behavior, meaning that each subsequent orbit shifts slightly relative to the previous one [56,57]. Conversely, if q is rational, the orbit is periodic, allowing a particle to return to its initial position after a finite number of revolutions. This classification not only enhances our understanding of BH dynamics, but also has potential applications in simplifying gravitational wave calculations by leveraging the properties of periodic orbits. The precessing orbit of a particle can be understood as a perturbation of a periodic orbit, which suggests that an analysis of periodic orbits may yield important insights into their characteristics, particularly in the context of BH physics. Kerr BHs are rotating BHs defined by their mass and angular momentum, with the surrounding spacetime displaying frame-dragging phenomena. Black holes of this type possess an ergosphere and a ring-shaped singularity, in contrast to non-rotating BHs. These models are essential for comprehending rotating compact objects within the framework of general relativity [58,59]. This classification approach has been rigorously explored across various BH

types, including Kerr metrics which are rotating and exhibit unique features such as an ergosphere and a static limit [60–62], Schwarzschild geometries which are non-rotating [63], charged BHs [64], naked singularities [65], polymer BHs [66], and others [67,68]. Some other interesting works on compact stellar models have been actively discussed, where different BH solutions are considered as exterior spacetime [69–95].

The study of hairy BHs is crucial for enhancing our understanding of BH properties and their physical characteristics. The hairy BH model challenges the traditional no-hair theorem, suggesting that these BHs can possess additional defining parameters, thus enriching the physical insights we can derive from them [96,97]. This complexity makes the examination of periodic orbits particularly significant, as they are sensitive to the physical influences exerted by the extra hairy parameters [98,99]. In the context of extreme-mass-ratio inspiral systems, time-like test particles that traverse the periodic orbits around hairy BHs will generate distinctive gravitational wave signals, which hold significant observational value for testing and extending the no-hair theorem. Moreover, these systems are crucial targets for upcoming gravitational wave detection initiatives, including LISA [100] and others [101,102]. The gravitational wave signals produced by binary systems provide crucial insights into the spacetime geometry surrounding BHs, enabling researchers to differentiate between standard BHs and those with "hair" or additional features. Analyzing the periodic orbits and gravitational wave signatures associated with hairy BHs enhances our understanding of these enigmatic objects and establishes a robust theoretical framework for interpreting data from future gravitational wave detections. This research not only enriches our understanding of BH physics, but also informs the design of upcoming observational strategies aimed at capturing these elusive cosmic phenomena. As one of the numerous extended theories of gravity, $f(R)$ gravity [80–84] is a popular alternative to GR. It modifies the gravitational action by adding a function of the Ricci scalar, R [85,86]. This theory aims to explain the universe's rapid expansion without the need for dark energy [87,88]. The focus of some research on this topic has been on analyzing the effects of this change on various astrophysical structures, particularly BHs [89,90]. An additional use of $f(R)$ gravity is its impact on spacetime geometry close to BHs [91,92], which changes how particle trajectories and QPOs respond [93,94].

This paper discusses the regular hairy BH and the particle dynamics around it. The paper is structured as follows. Section 2 considers the line element that represents the geometry of a non-singular hairy BH and defines certain parameters associated with this geometry. Section 3 discusses the dynamics of those particles surrounded by the hairy BH. In this regard, we explore the effective potential, innermost stable circular orbits, the particles' trajectories in which they move, and the impact of the hairy parameter on the effective force. Section 4 explores the perturbations of the circular orbit and the harmonic oscillations it produces. We also explore the frequencies of moving particles measured by both local and distant observers. In the final section, we conclude our results in light of how the parameter α significantly influences the dynamics of the particles.

2 Hairy regular BH

The line element describing the geometry of a spherically symmetric hairy regular BH is given by [103]:

$$\mathrm{d}s^2 = -f(r)\mathrm{d}t^2 + f^{-1}(r)\mathrm{d}r^2 + r^2(\mathrm{d}\theta^2 + \sin^2\theta\mathrm{d}\phi^2), \quad (1)$$

where the lapse function $f(r)$ reads

$$f(r) = 1 + \frac{1}{Mr}\left(2M^2 + \frac{2Mr}{\alpha} + \frac{r^2}{\alpha^2}\right) \times \exp\left(-\frac{r}{\alpha M}\right) - \frac{2M}{r}. \quad (2)$$

Here, M is the mass of the BH, and α is a hairy parameter of the BH model. In contrast to other hairy solutions, the current considered regular hairy black hole is distinguished by its ability to avoid singularities and maintain secondary hair by using the parameter α. We would like to mention here that it is very easy to obtain Schwarzschild geometries by taking $\alpha \to 0$, where in a straightforward way one can obtain the Minkowski spacetime by imposing a condition $\alpha \to \infty$. The horizon of the non-rotating hairy regular BH (1) can be found by solving $f(r) = 0$. The behavior of parameters α on the lapse function $f(r)$ is illustrated in Fig. 1. It can be seen that the lapse function increases with increasing radial distance r and hairy parameter α. The function $f(r)$ crosses the axis of $0 < \alpha \leq 0.387$. Thus, BH exists when $0 < \alpha \leq 0.387$.

3 Particle dynamics around a hairy regular BH

The following equations represent the Hamiltonian of a neutral particle's motion:

$$H = \frac{1}{2}g^{\mu\nu}p_\mu p_\nu + \frac{1}{2}\mu^2, \quad (3)$$

where μ is the particle's mass, $p^\alpha = \mu u^\alpha$, $u^\alpha = \mathrm{d}x^\alpha/\mathrm{d}\tau$ is the four-velocity, and τ is the proper time associated with the particle. It is possible to express the equations of motion in Hamiltonian formalism as

$$\frac{\mathrm{d}x^\alpha}{\mathrm{d}\zeta} \equiv \mu u^\alpha = \frac{\partial H}{\partial p_\alpha}, \quad \frac{\mathrm{d}p_\alpha}{\mathrm{d}\zeta} = -\frac{\partial H}{\partial x^\alpha}, \quad (4)$$

where the affine parameter is $\zeta = \tau/\mu$.

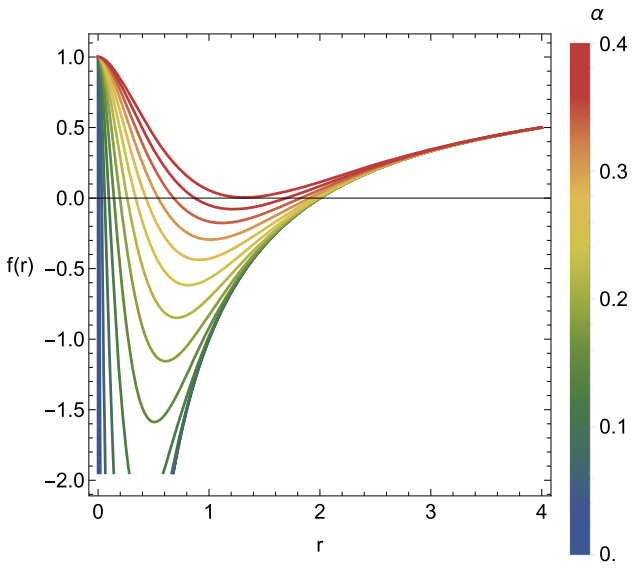

Fig. 1 Behavior of the lapse function of spacetime of a non-rotating hairy regular BH

The inherent symmetries of geometry give rise to two conserved quantities, the specific angular momentum L and the specific energy E, which are stated as

$$\frac{p_t}{m} = 1 + \frac{1}{Mr}\left(2M^2 + \frac{2Mr}{\alpha} + \frac{r^2}{\alpha^2}\right) \times \exp\left(-\frac{r}{\alpha M}\right) - \frac{2M}{r} = -\mathcal{E}, \tag{5}$$

$$\frac{p_\phi}{m} = r^2 \sin^2\theta \frac{\mathrm{d}\phi}{\mathrm{d}\tau} = \mathcal{L}, \tag{6}$$

where $\mathcal{E} = E/m$ and $\mathcal{L} = L/m$ are the definitions of specific energy and specific angular momentum, respectively.

The equations of motion that follow the temporal u^t, azimuthal u^ϕ, and radial u^r components of the four-velocity u^α components are as follows:

$$\dot{t} = \frac{\mathcal{E}}{\left(1 + \frac{1}{Mr}\left(2M^2 + \frac{2Mr}{\alpha} + \frac{r^2}{\alpha^2}\right)\exp\left(-\frac{r}{\alpha M}\right) - \frac{2M}{r}\right)}, \tag{7}$$

$$\dot{\phi} = \frac{\mathcal{L}}{r^2 \sin^2\theta}, \tag{8}$$

$$\dot{r}^2 + \left(\epsilon + \frac{\mathcal{L}^2}{r^2\sin^2\theta}\right)\left(1 + \frac{1}{Mr}\left(2M^2 + \frac{2Mr}{\alpha} + \frac{r^2}{\alpha^2}\right)\exp\left(-\frac{r}{\alpha M}\right) - \frac{2M}{r}\right) = \mathcal{E}^2, \tag{9}$$

where $\epsilon = 1$ denotes time-like particles while $\epsilon = 0$ denotes null particles in this context. The overdot represents a difference in relation to the correct time τ.

The Hamiltonian (3) for a non-rotating hairy regular BH (1) can be written in the form

$$H = \frac{1}{2}\left[1 + \frac{1}{Mr}\left(2M^2 + \frac{2Mr}{\alpha} + \frac{r^2}{\alpha^2}\right)\exp\left(-\frac{r}{\alpha M}\right) - \frac{2M}{r}\right] p_r^2 + \frac{1}{2r^2}p_\theta^2 + \frac{1}{2}\frac{m^2}{f(r)}\left[V_{\text{eff}}(r,\theta) - \mathcal{E}^2\right], \tag{10}$$

where the effective potential $V_{eff}(r,\theta)$ takes the form

$$V_{eff}(r,\theta) = \left(1 + \frac{\mathcal{L}^2\csc^2\theta}{r^2}\right)\left(1 + \frac{1}{Mr}\left(2M^2 + \frac{2Mr}{\alpha} + \frac{r^2}{\alpha^2}\right) \times \exp\left(-\frac{r}{\alpha M}\right) - \frac{2M}{r}\right). \tag{11}$$

For $\alpha = 0$, the effective potential (11) reduces to the Schwarzschild case.

3.1 Effective potential

The effective potential $V_{eff}(r,\theta)$ is crucial for examining the motion of test particles, as it facilitates the analysis of particle trajectories without the need to directly solve the equations of motion. The extrema of V_{eff} elucidate orbital stability: peaks signify unstable circular orbits, whereas minima denote stable circular orbits. Figure 2 shows the variation in V_{eff} with respect to the radial coordinate r. Stable orbits correspond to the minima of the potential, while unstable orbits are related to its maximum. An increase in the hairy parameter α or the orbital angular momentum $\mathcal{L}$ increases the effective potential. Furthermore, when α increases, the potential's minimum approaches the event horizon.

The circular orbits for an equatorial plane are found under the following conditions:

$$V_{\text{eff}}(r) = \mathcal{E}^2, \quad \frac{\mathrm{d}V_{\text{eff}}(r)}{\mathrm{d}r} = 0. \tag{12}$$

To solve Eq. (12), we obtain the circular orbits around a non-rotating hairy regular BH, given by

$$\mathcal{L} = \frac{r\sqrt{2 - \frac{e^{-\frac{r}{\alpha}}(\alpha+r)(2\alpha^2+r^2)}{\alpha^3}}}{\sqrt{\frac{e^{-\frac{r}{\alpha}}(6\alpha^3+r^3+3\alpha r^2+6\alpha^2 r)}{\alpha^3} + 2(r-3)}}, \tag{13}$$

and the corresponding energy takes the form

$$\mathcal{E} = \frac{\sqrt{2}e^{-\frac{r}{\alpha}}\left(r^2 - 2\alpha^2\left(e^{r/\alpha} - 1\right) + \alpha r\left(\alpha e^{r/\alpha} + 2\right)\right)}{\alpha^2\sqrt{\frac{re^{-\frac{r}{\alpha}}\left(r^3+3\alpha r^2-6\alpha^3\left(e^{r/\alpha}-1\right)+2\alpha^2 r\left(\alpha e^{r/\alpha}+3\right)\right)}{\alpha^3}}}. \tag{14}$$

Figure 3 illustrates the angular momentum $\mathcal{L}$ for equatorial circular orbits surrounding a non-rotating hairy regular BH. However, the angular momentum $\mathcal{L}$ decreases as the hairy parameter α increases, increasing with a greater radial distance. The circular orbits around a conventional

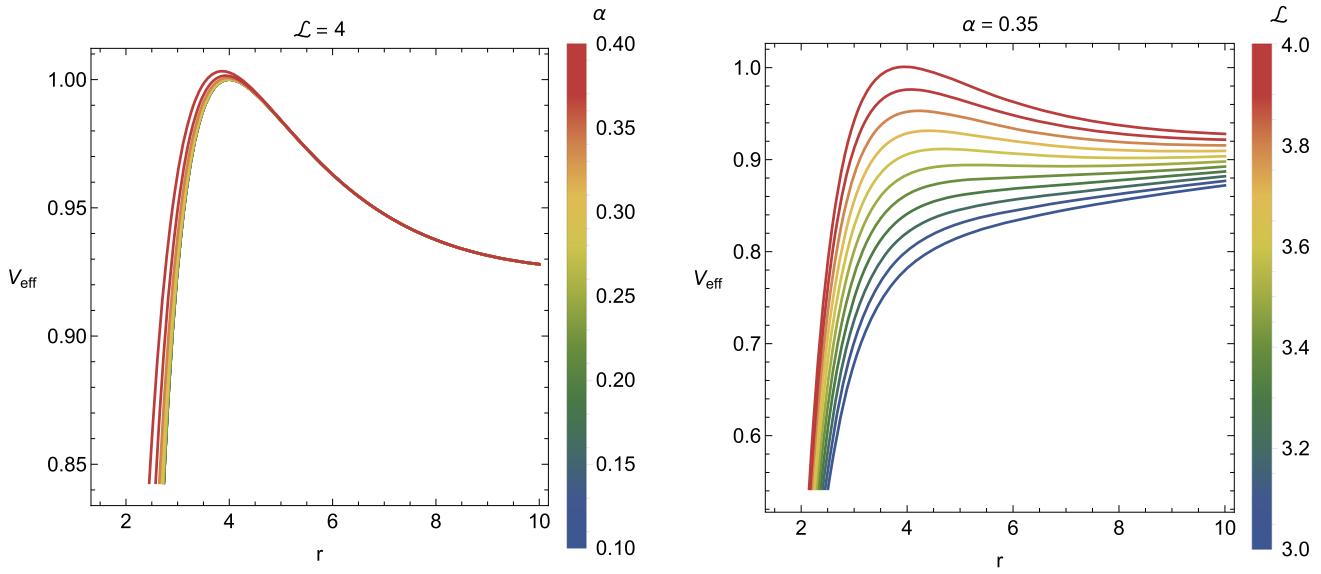

Fig. 2 Plots of the effective potential of particles around a non-rotating hairy regular BH

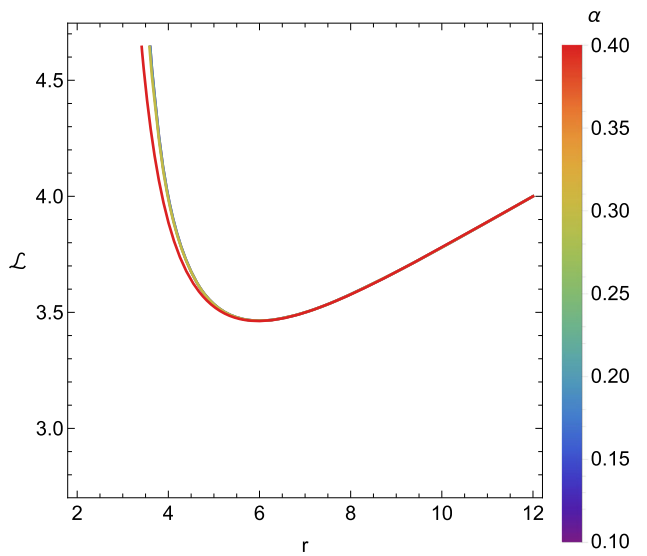

Fig. 3 Plots of angular momentum of particles moving around a non-rotating hairy regular BH

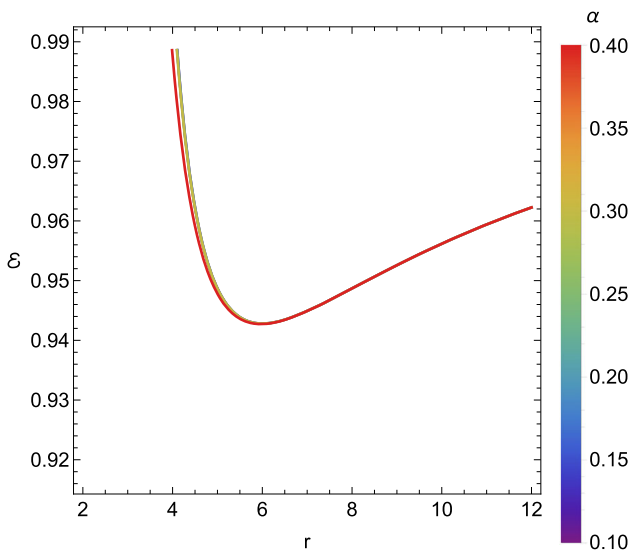

Fig. 4 Plots of energy of particles moving around a non-rotating hairy regular BH

Schwarzschild solution demonstrate greater angular momentum than those around a hairy regular BH solution. Figure 4 presents the energy $\mathcal{E}$ of equatorial circular orbits around a non-rotating hairy regular BH. As the hairy parameter α increases, the energy of the particles decreases. In contrast, the energy increases with the radial distance r.

3.2 Innermost stable circular orbits

Stable and unstable circular orbits are distinguished by the minima and maxima of the effective potential, respectively. In Newtonian physics, the effective potential consistently exhibits a minimum for any given angular momentum, and there is no notion of an innermost stable circular orbit (ISCO) with a specified minimum radius. Nevertheless, the effective potential is contingent upon the particle's rotational momentum and additional parameters. At a particular angular momentum, these two extrema converge, establishing the ISCOs, situated at $r = 3r_g$, where r_g represents the Schwarzschild radius. The ISCOs for the considered BH can be ascertained by employing the subsequent criteria

$$\frac{\mathrm{d}^2 V_{\text{eff}}(r)}{\mathrm{d}\, r^2} = 0. \tag{15}$$

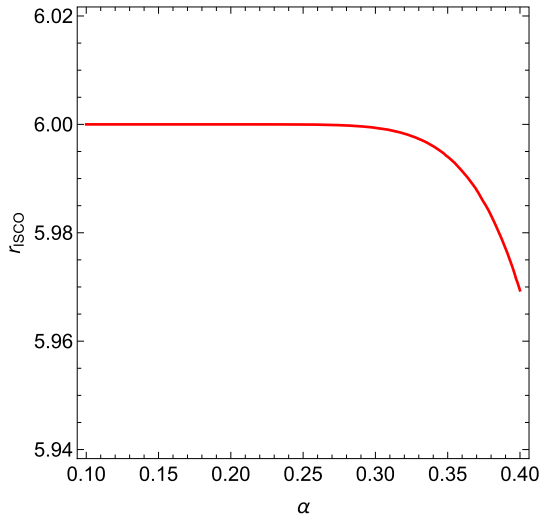

Fig. 5 Plots for ISCOs of particles moving around non-rotating hairy regular BH

The radius of an ISCO for a non-rotating hairy regular BH is given by

$$e^{-\frac{r}{\alpha}}\Big(-r^6+\alpha r^5\left(\alpha e^{r/\alpha}-5\right)-\alpha^2 r^4\left((3\alpha+2)e^{r/\alpha}+15\right)$$
$$-\alpha^3 r^3\left((\alpha-14)e^{r/\alpha}+26\right)-2\alpha^4 r^2\left((\alpha-6)e^{r/\alpha}+12\right)$$
$$-12\alpha^6\left(e^{r/\alpha}-1\right)^2+2\alpha^5 r\left(e^{r/\alpha}-1\right)\left(\alpha e^{r/\alpha}+12\right)\Big)=0. \quad (16)$$

Figure 5 illustrates the equatorial ISCOs around a non-rotating hairy regular BH. The parameter α modifies the gravitational potential, reducing the ISCO radius by allowing stable orbits closer to the black hole. Initially, the ISCOs' radii remain constant with increasing hairy parameter α and then decrease as α increases. For the case where $\alpha = 0$, the ISCO radius is found to be $r_{\rm ISCO} = 6$. The ISCOs around a hairy regular BH lie below the ISCOs corresponding to a classical Schwarzschild BH. They significantly influence the efficiency of energy extraction from the atmosphere and the dynamics of accreting matter. The ISCOs affect the luminosity and spectral characteristics of X-ray binaries and active galactic nuclei. Researchers can estimate their mass and spin by analyzing X-ray emissions and their spectra. The energy and structure of the X-ray emission lines help to elucidate the location of the ISCOs.

3.3 Trajectories of particles around a BH

We numerically solve the equations of motion for test particles and plot their trajectories around a non-rotating hairy regular BH, depicted in Fig. 6. Different trajectories are plotted for varying hairy parameters α. The first row represents the case with $\alpha = 0.1$, the second row for $\alpha = 0.2$, and the third row for $\alpha = 0.39$. We fix all parameters and vary the hairy parameter α, and examine the effects of varying α on particle trajectories. All the cases result in stable motion. Increasing the hairy parameter α shifts the particle motion closer to the BH event horizon.

3.4 Effective force

The effective force acting on a particle provides clarity with respect to its motion, indicating whether it is being attracted to the BH or repelled from it. We examine the dynamics of particles in the vicinity of a non-rotating hairy regular black hole, where both attractive and repulsive gravitational forces may occur. The resulting force exerted on the particle is obtained using Eq. (12), articulated as

$$F=-\frac{1}{2}\frac{dV_{eff}}{dr} \quad (17)$$
$$=\frac{e^{-\frac{r}{\alpha}}\left(\mathcal{L}^2\left(r^3+3\alpha r^2-6\alpha^3\left(e^{r/\alpha}-1\right)+2\alpha^2 r\left(\alpha e^{r/\alpha}+3\right)\right)+r^2\left(r^3+\alpha r^2-2\alpha^3\left(e^{r/\alpha}-1\right)+2\alpha^2 r\right)\right)}{2\alpha^3 r^4}. \quad (18)$$

Figure 7 illustrates how the effective force varies with r for different sets of BH parameters. As the hairy parameter α increases, the effective force becomes more attractive. Similarly, smaller values of the orbital angular momentum of the particle result in a more attractive force. Moreover, the effective force increases with increasing values of the hairy parameter α or the angular momentum $\mathcal{L}$.

4 Harmonic oscillations as perturbation of circular orbits

To examine the oscillatory motion of neutral particles, we applied perturbations to the equations of motion surrounding stable circular orbits. Upon a minor displacement of a test particle from its equilibrium location in a stable circular orbit inside the equatorial plane, it experiences epicyclic motion, defined by linear harmonic oscillations.

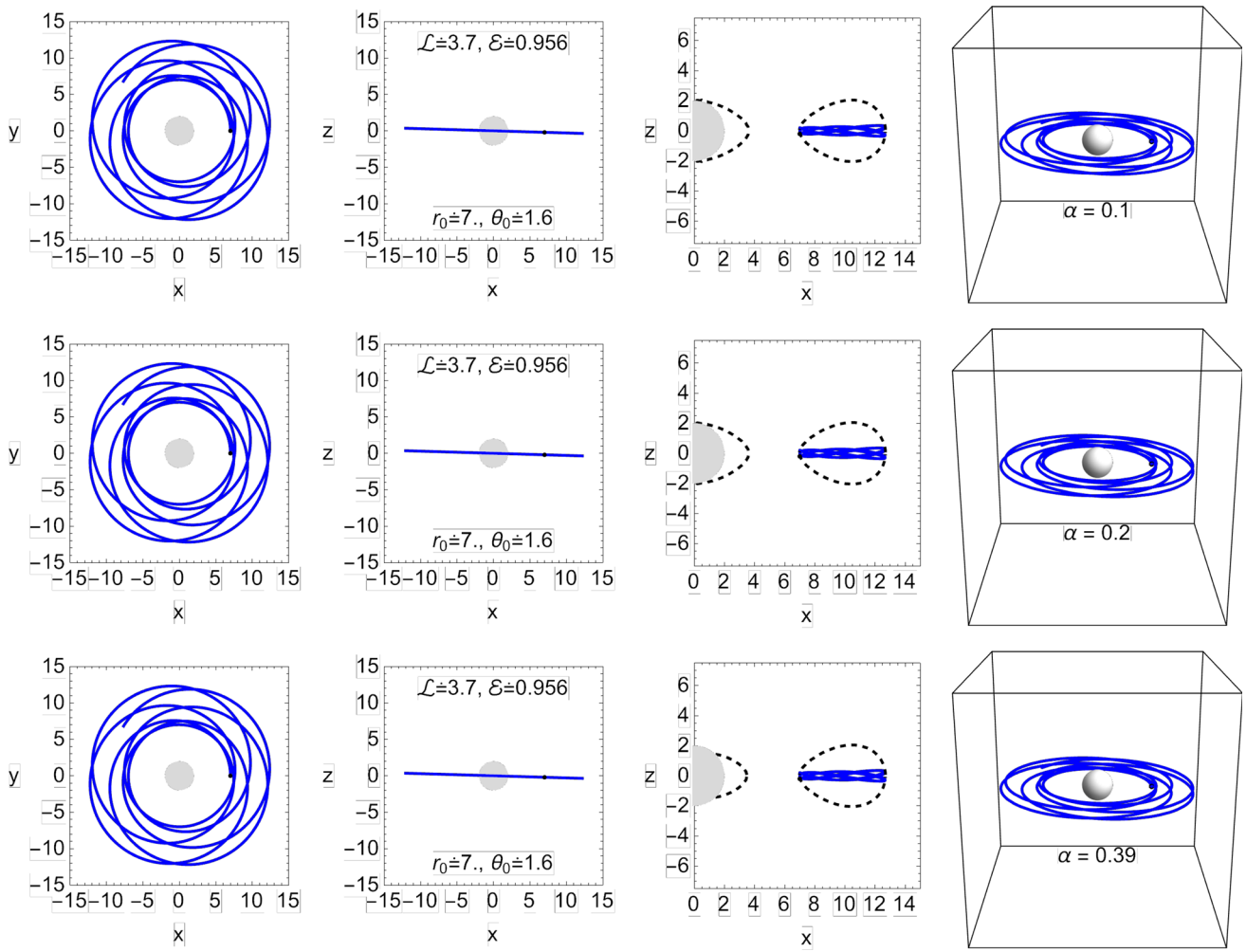

Fig. 6 Trajectories of test particles moving around a non-rotating hairy regular BH

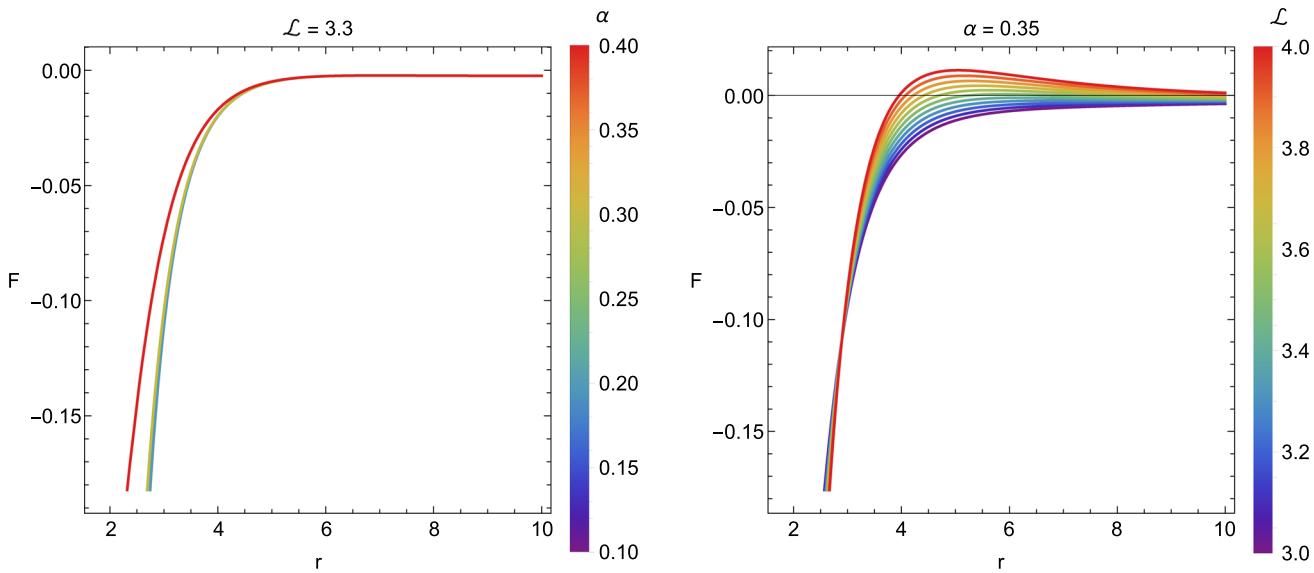

Fig. 7 Plots for the effective force acting on particles moving around a non-rotating hairy regular BH

4.1 Frequencies measured by a local observer

The frequencies of harmonic oscillatory motion ascertained by the local observer are specified as follows:

$$\omega_r^2 = \frac{-1}{2}\frac{\partial^2 V_{\rm eff}(r,\theta)}{\partial r^2}, \tag{19}$$

$$\omega_\theta^2 = \frac{1}{2}\frac{g_{rr}(r,\theta)}{r^2}\frac{\partial^2 V_{\rm eff}(r,\theta)}{\partial \theta^2}, \tag{20}$$

$$\omega_\phi = \frac{{\rm d}\phi}{{\rm d}\tau}. \tag{21}$$

The radial (ω_r), latitudinal (ω_θ), and orbital/axial (ω_ϕ) frequencies of the neutral test particle for a non-rotating hairy regular BH take the following form:

$$\begin{aligned}\omega_r^2 = \frac{e^{-\frac{r}{\alpha}}}{2\alpha^4 r^5}\Big[&-\Big(\mathcal{L}^2\left(r^4+4\alpha r^3+12\alpha^2 r^2-24\alpha^4\left(e^{r/\alpha}-1\right)\right.\\ &\left.+6\alpha^3 r\left(\alpha e^{r/\alpha}+4\right)\right)\Big)\\ &-r^2\left(r^4+2\alpha^2 r^2-4\alpha^4\left(e^{r/\alpha}-1\right)+4\alpha^3 r\right)\Big],\end{aligned} \tag{22}$$

$$\omega_\theta^2 = \frac{2-\frac{e^{-\frac{r}{\alpha}}(\alpha+r)\left(2\alpha^2+r^2\right)}{\alpha^3}}{r^2\left(\frac{e^{-\frac{r}{\alpha}}\left(6\alpha^3+r^3+3\alpha r^2+6\alpha^2 r\right)}{\alpha^3}+2(r-3)\right)}, \tag{23}$$

$$\omega_\phi^2 = \frac{2-\frac{e^{-\frac{r}{\alpha}}(\alpha+r)\left(2\alpha^2+r^2\right)}{\alpha^3}}{r^2\left(\frac{e^{-\frac{r}{\alpha}}\left(6\alpha^3+r^3+3\alpha r^2+6\alpha^2 r\right)}{\alpha^3}+2(r-3)\right)}. \tag{24}$$

For vanishing parameters $\alpha = 0$, the Eqs. (22)–(24) reduce to the radial, latitudinal, and axial frequencies of test particles around a non-rotating Schwarzschild BH.

4.2 Frequencies measured by a distant observer

The locally determined angular frequencies ω_β are specified in Eqs. (22)–(24). In contrast, the angular frequencies as measured by a static distant observer (Ω) are given by

$$\Omega_\beta = \omega_\beta \frac{{\rm d}\tau}{{\rm d}t}, \tag{25}$$

where ${\rm d}\tau/{\rm d}t$ is the redshift coefficient, given by

$$\frac{{\rm d}t}{{\rm d}\tau} = -\frac{\mathcal{E}}{g_{tt}}. \tag{26}$$

When a distant observer measures the frequencies of small harmonic oscillations in physical units, the frequencies of neutral particles, as ascertained by these observers, manifest as follows:

$$\nu_i = \frac{1}{2\pi}\frac{c^3}{GM}\Omega_i[{\rm Hz}], \tag{27}$$

where $i \in \{r,\theta,\phi\}$; Ω_r, Ω_θ, and Ω_ϕ denote the dimensionless radial, latitudinal, and axial angular frequencies as perceived by a distant observer and are defined as follows:

$$\begin{aligned}\Omega_r^2 = \frac{e^{-\frac{2r}{\alpha}}}{2\alpha^6 r^4}\Big[&-r^6+\alpha r^5\left(\alpha e^{r/\alpha}-5\right)\\ &-\alpha^2 r^4\left((3\alpha+2)e^{r/\alpha}+15\right)\\ &-\alpha^3 r^3\left((\alpha-14)e^{r/\alpha}+26\right)\\ &-2\alpha^4 r^2\left((\alpha-6)e^{r/\alpha}+12\right)\\ &-12\alpha^6\left(e^{r/\alpha}-1\right)^2+2\alpha^5 r\left(e^{r/\alpha}-1\right)\\ &\times\left(\alpha e^{r/\alpha}+12\right)\Big],,\end{aligned} \tag{28}$$

$$\Omega_\theta^2 = \frac{e^{-\frac{r}{\alpha}}\left(-r^3-\alpha r^2+2\alpha^3\left(e^{r/\alpha}-1\right)-2\alpha^2 r\right)}{2\alpha^3 r^3}, \tag{29}$$

$$\Omega_\phi^2 = \frac{e^{-\frac{r}{\alpha}}\left(-r^3-\alpha r^2+2\alpha^3\left(e^{r/\alpha}-1\right)-2\alpha^2 r\right)}{2\alpha^3 r^3}. \tag{30}$$

Figure 8 presents the radial profiles of the frequencies ν_j for small harmonic oscillations of neutral particles around a non-rotating hairy regular BH, observed by a distant observer. Frequencies are plotted for different values of the hairy parameter α. The radial profiles of the orbital frequency (Ω_ϕ) and the latitudinal frequency (Ω_θ) overlap. The radial profiles do not change much when increasing the hairy parameter α. Moreover, the frequencies of QPOs can be associated with the orbital frequencies of matter in proximity to the ISCOs, especially around them. If the inner border of the accretion disk is situated at or near the ISCOs, the frequencies of the QPOs may be linked to the dynamics of the disk material orbiting at this radius under the effect of the involved parameter α. The currently calculated QPOs can be detected by X-ray observations.

4.3 Periastron precession

This section examines the periastron frequency of a neutral test particle circling a non-rotating hairy regular BH, concentrating on minor perturbations around the equatorial plane at $\pi/2$. To determine periastron precession, we examine a minor variation in the particle from its equilibrium location, leading to oscillations around that point, characterized by a radial frequency Ω_r. The periastron frequency, represented as Ω_P, is defined as the differential between the orbital frequency Ω_ϕ and the radial frequency Ω_r, expressed by the following relation:

$$\Omega_P = \Omega_\phi - \Omega_r, \tag{31}$$

$$\begin{aligned}\Omega_P = \sqrt{\frac{e^{-\frac{r}{\alpha}}\left(-r^3-\alpha r^2+2\alpha^3\left(e^{r/\alpha}-1\right)-2\alpha^2 r\right)}{2\alpha^3 r^3}}\\ -\frac{e^{-\frac{r}{\alpha}}}{2\alpha^3 r^2}\Big[-r^6+\alpha r^5\left(\alpha e^{r/\alpha}-5\right)\\ -\alpha^2 r^4\left((3\alpha+2)e^{r/\alpha}+15\right)\\ -\alpha^3 r^3\left((\alpha-14)e^{r/\alpha}+26\right)\end{aligned}$$

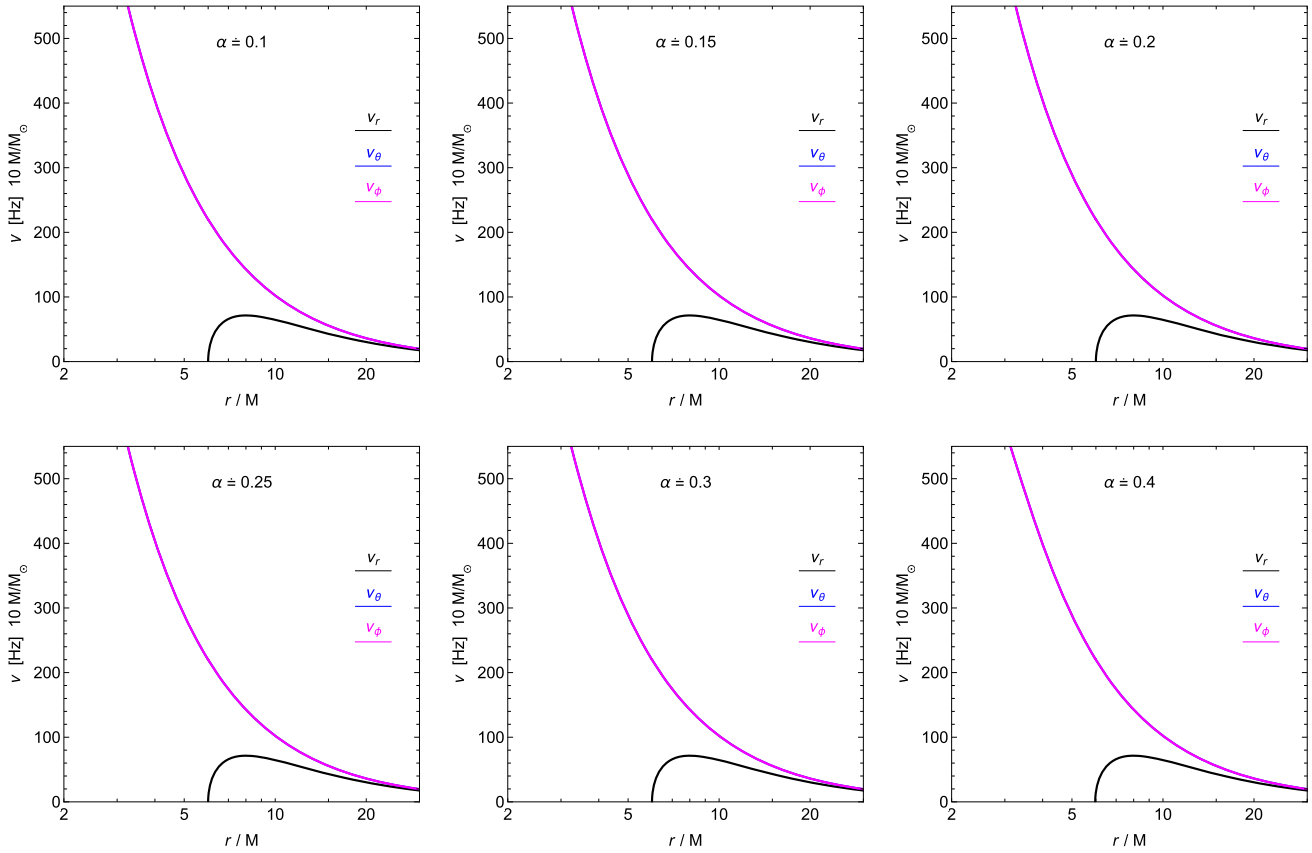

Fig. 8 Plots of frequencies of particles moving in the background of a non-rotating hairy regular BH

$$-2\alpha^4 r^2\left((\alpha-6)e^{r/\alpha}+12\right) -12\alpha^6\left(e^{r/\alpha}-1\right)^2+2\alpha^5 r\left(e^{r/\alpha}-1\right) \left(\alpha e^{r/\alpha}+12\right)\Big]^{\frac{1}{2}}. \tag{32}$$

Unlike Newtonian gravity, where the radial and orbital frequencies are equal, general relativistic effects near a BH lead to the inequality $\Omega_\theta \neq \Omega_\phi$. Figure 9 presents the graphical behavior of the periastron frequency for particles orbiting a non-rotating hairy regular BH, showing the effects of varying BH parameter α. The frequency of the periastron decreases as the radial distance increases. Moreover, as the hairy parameter α increases, the frequency of the periastron decreases.

5 Constraints on the parameters of a decoupling black hole

This section presents constraints on the parameters of a gravitational decoupling BH using QPO observations from different binary X-ray systems. We employ Markov chain Monte Carlo (MCMC) sampling to explore the parameter space, leveraging the emcee software package for posterior distribution estimation. The analysis incorporates multi-frequency QPO data from these systems to investigate deviations from standard predictions, focusing in particular on hairy parameters arising from the considered BH solution. The selected binaries provide complementary constraints through their well-measured twin-peak QPO frequencies, which probe different orbital resonance conditions in the strong-field regime, particularly the relativistic precession (RP) model. The twin-peak QPOs observed in many X-ray binaries are interpreted within the RP model as follows:

$$\nu_U = \nu_\phi, \quad \text{(Upper QPO frequency)} \tag{33}$$

$$\nu_L = \nu_\phi - \nu_r. \quad \text{(Lower QPO frequency)} \tag{34}$$

This model naturally explains the observed 3:2 frequency ratio in high-frequency QPOs (HFQPOs) as a resonance condition between these fundamental oscillatory modes [104,105].

5.1 Markov chain Monte Carlo

In this phase of the study, the MCMC methodology is implemented to rigorously estimate the physical parameters that govern the decoupling BH system. The analysis leverages the relativistic precession framework, which incor-

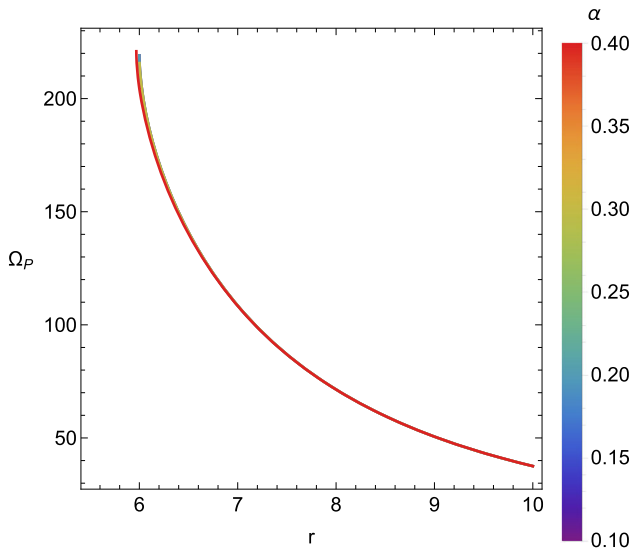

Fig. 9 Plots for periastron frequency of particles moving around a non-rotating hairy regular BH

porates orbital dynamics influenced by strong-field gravitational effects. Posterior probability distributions are systematically constructed through Bayesian inference, integrating observational data with theoretical priors to quantify parameter uncertainties. This approach enables high-precision sampling of the multidimensional parameter space, ensuring robustness against local minima and convergence to physically meaningful solutions. The formulation of this distribution is given by

$$\mathcal{P}(\Theta \mid \mathcal{D}, \mathcal{M}) = \frac{L(\mathcal{D} \mid \Theta, \mathcal{M})\pi(\Theta \mid \mathcal{M})}{Z(\mathcal{D} \mid \mathcal{M})}. \tag{35}$$

In Bayesian inference, the posterior distribution $\mathcal{P}(\Theta \mid \mathcal{D}, \mathcal{M})$ captures the updated probability distribution of model parameters Θ after conditioning on observed data $\mathcal{D}$ and assuming a specific model structure $\mathcal{M}$. This distribution arises from the interaction of two key components: the likelihood function $L(\mathcal{D} \mid \Theta, \mathcal{M})$, which quantifies the probability of observing the dataset $\mathcal{D}$ under fixed parameters Θ and the model $\mathcal{M}$, and the prior distribution $\pi(\Theta \mid \mathcal{M})$, which encapsulates prior assumptions or beliefs about the values of plausible parameters before observing the data. The posterior is proportional to the product of these two components, scaled by the normalization factor $Z(\mathcal{D} \mid \mathcal{M})$, often referred to as the model evidence. This marginal likelihood ensures probabilistic coherence by integrating the product of the likelihood and prior over the entire parameter space, thereby guaranteeing that the posterior constitutes a valid probability density function.

In our model, the prior distributions are specified as Gaussian within predefined limits, with the constraint given by

$$\pi(\theta_i) \sim \exp\left[-\frac{1}{2}\left(\frac{\theta_i - \theta_{0,i}}{\sigma_i}\right)^2\right], \quad \theta_{\text{low},i} < \theta_i < \theta_{\text{high},i}. \tag{36}$$

This applies to the parameters $\theta_i = [M, r, \alpha, \beta]$, each associated with its respective standard deviation σ_i. To facilitate a more nuanced analysis, we utilize dimensionless variables α/M, β/M, and $r = r_{3:2}/M$, which represent the normalized radial position of the 3:2 resonance. Our MCMC analysis integrates five different datasets derived from both higher- and lower-frequency data presented in Table 1. The likelihood function, denoted as $\mathcal{L}$, forms the central component of this analysis and is formulated accordingly as

$$\log \mathcal{L} = \log \mathcal{L}_{\text{up}} + \log \mathcal{L}_{\text{low}}. \tag{37}$$

The logarithmic form of the likelihood function is constructed by summing the logarithms of the likelihoods associated with both the high- and low-frequency data. Specifically, the logarithm of $\mathcal{L}_{\text{up}}$ encapsulates the likelihood pertaining to the high-frequency data, which is mathematically represented as

$$\log \mathcal{L}_{\text{up}} = -\frac{1}{2}\sum i \left(\frac{(\nu^i_{\text{up, obs}} - \nu^i_{\text{up, th}})^2}{(\sigma^i_{\text{up, obs}})^2}\right). \tag{38}$$

Conversely, $\log \mathcal{L}_{\text{low}}$ denotes the likelihood linked to the low-frequency data and is formulated as

$$\log \mathcal{L}_{\text{low}} = -\frac{1}{2}\sum i \left(\frac{(\nu^i_{\text{low, obs}} - \nu^i_{\text{low, th}})^2}{(\sigma^i_{\text{low, obs}})^2}\right). \tag{39}$$

This approach enables the estimation of Θ for the considered BH model using the observed dataset $\mathcal{D}$ within the framework of the model $\mathcal{M}$, thus facilitating a comprehensive analysis of the underlying phenomena. Harmonic oscillations can be seen as minor deviations from stable circular orbits in various physical systems, including the cases of the planetary motion and charged particles in magnetic fields. When an item significantly diverges from a circular trajectory, the restoring forces exerted on it frequently induce oscillatory motion, which can be approximated as harmonic. These perturbations generally manifest in the radial or vertical direction and are regulated by linearized equations of motion. This method streamlines the examination of stability and resonances in dynamical systems. The constraining bonds using the observational data for four different pulsars on the involved parameters can be seen in Fig. 10. The best-fit values for the parameters are provided in Table 2.

Table 1 Key characteristics of the five X-ray binary systems selected for our analysis, including their masses, upper frequencies, and lower frequencies of QPOs

	GRO J1655-40	XTE J1550-564	XTE J1859+226	GRS 1915+105
$M\ (M_{\odot})$	5.4 ± 0.3	9.1 ± 0.61	7.85 ± 0.46	$12.4^{+2.0}_{-1.8}$
ν_{up}(Hz)	441 ± 2	276 ± 3	$227.5^{+2.1}_{-2.4}$	168 ± 3
ν_{low}(Hz)	298 ± 4	184 ± 5	$128.6^{+1.6}_{-1.8}$	113 ± 5

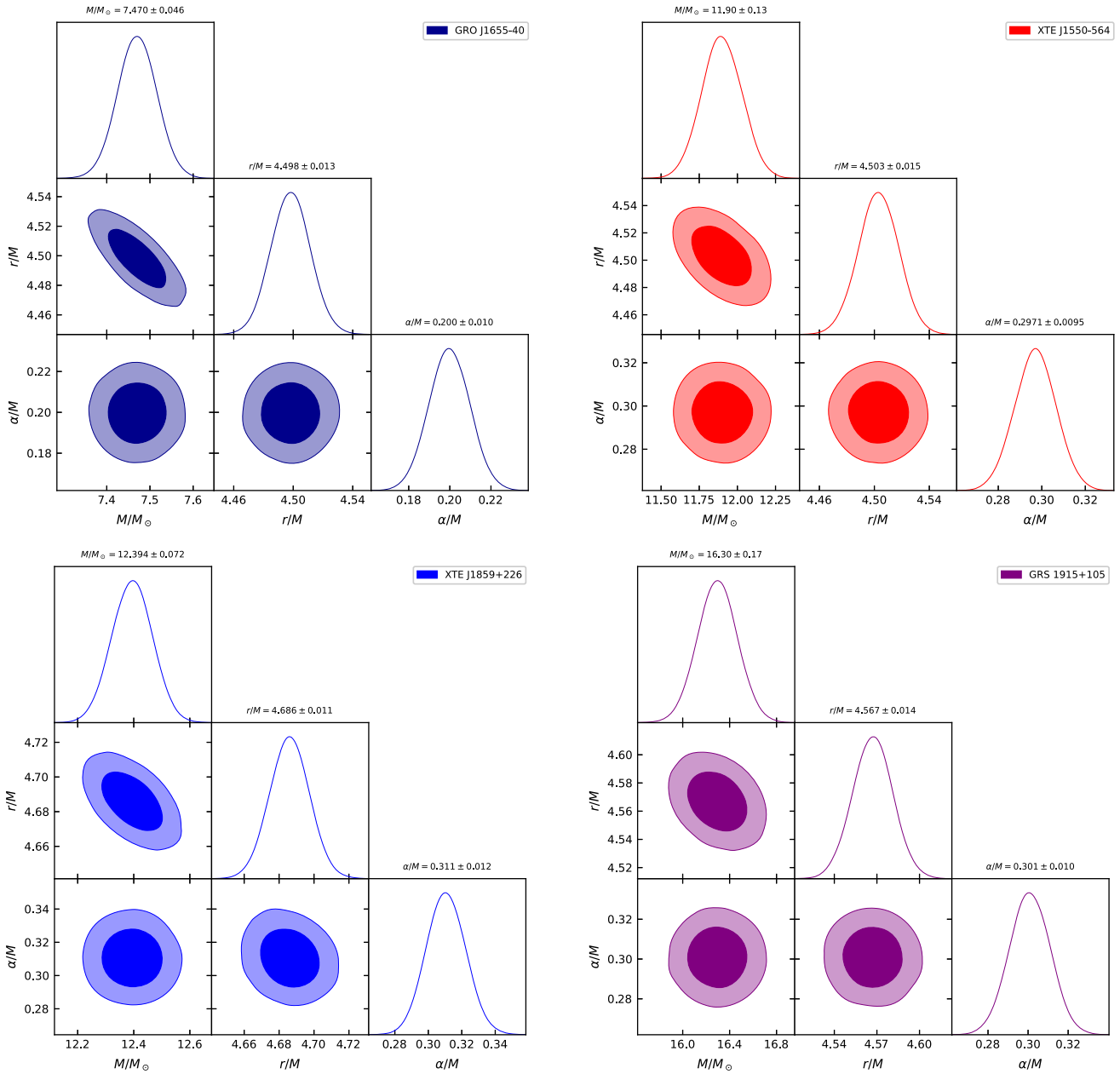

Fig. 10 Parameter constraints obtained from various observational data measurements within the framework of the model, showing both 1σ and 2σ confidence intervals

Table 2 Constraints at 95% CL on the parameters for the decoupling BH using different QPO measurements

Object	$M/M_{\odot}$	r/M	α/M
GRO J1655-40	7.470±0.046	4.498±0.013	0.200±0.010
XTE J1550-564	11.90±0.13	4.503±0.015	0.2971±0.0095
XTE J1859+226	12.394±0.072	4.686±0.011	0.311±0.012
GRS 1915+105	16.30±0.17	4.567±0.014	0.301±0.010

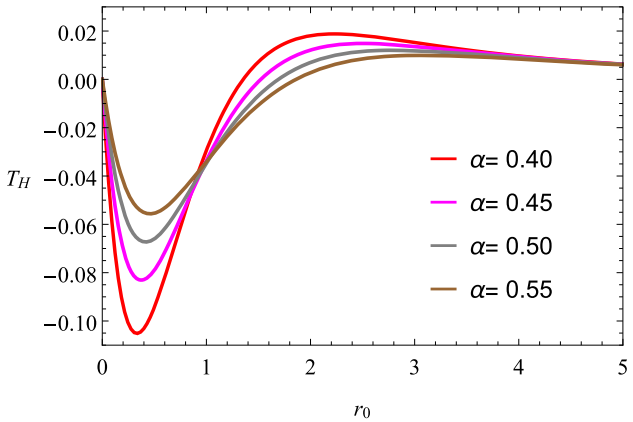

Fig. 11 Hawking temperature T_H along horizon radius r_0 by fixing $M = 1$ for different values of α

6 Hawking temperature of a regular hairy black hole

Taking the derivative of $f(r)$ with respect to r allows us to derive the Hawking temperature T_H for regular hairy BHs, expressed as

$$T_H = \frac{e^{-\frac{r_0}{\alpha M}}\left(2\alpha^3 M^3\left(e^{\frac{r_0}{\alpha M}}-1\right)-2\alpha^2 M^2 r_0-\alpha M r_0^2-r_0^3\right)}{4\pi\alpha^3 M^2 r_0^2}. \tag{40}$$

In this context, $r = r_0$ denotes the BH event horizon. The thermodynamic stability of a system is significantly influenced by the sign of its temperature. Systems with positive temperatures generally exhibit stability because they can absorb energy to reach equilibrium without succumbing to runaway effects. In contrast, negative temperatures often indicate an unstable state characterized by an inverted population distribution. Typically, a positive temperature is necessary for achieving stability. In our analysis, the graphical representation of the Hawking temperature, as depicted in Fig. 11, reveals that for varying values of α, the regular BH solution initially exhibits instability due to negative temperatures. However, beyond a certain radius of horizon $r_0 > 1$, which depends on the specific values of α, the solution transitions to a positive temperature regime, thereby demonstrating the global stability of the regular hairy BH.

Our study employs Tsallis entropy due to its capacity to characterize systems demonstrating non-extensive behavior, especially in black hole thermodynamics, where conventional Boltzmann–Gibbs entropy may inadequately represent the system's inherent complexity. Tsallis entropy offers a more generalized framework for statistical mechanics by incorporating a parameter κ, which enables the entropy to consider non-equilibrium states and long-range interactions frequently encountered in gravitational systems. In some systems, like black holes, classical thermodynamics may not adequately characterize the microscopic states, especially under intense gravitational fields or severe circumstances. Hence, the Tsallis entropy of the BH is expressed in the following form [106]:

$$S = \delta\left(\pi r_0^2\right)^{\kappa}, \tag{41}$$

where κ regulates the degree of non-extensiveness, with $\kappa = 1$ corresponding to the classical entropy. For $\kappa \neq 1$, it encompasses nonlocal interactions or quantum corrections pertinent to gravitational systems, where δ is a scaling factor that guarantees the appropriate dimensionality and magnitude of the entropy, modifying the entropy according to the specific geometry or structure of the BH.

The examination of particle motion and the use of the Tsallis entropy in BH physics provide significant insights into the relationship between gravitational dynamics and thermodynamics. This study examines the motion of test particles around a spherically symmetric, non-rotating hairy regular BH, demonstrating the impact of BH parameters (mass M and hairy parameter α) on particle trajectories, the stability of circular orbits, and oscillatory behaviors. These findings enhance our understanding of BH spacetime geometry and its influence on particle dynamics, encompassing phenomena such as precession and stable orbital radii. The incorporation of Tsallis entropy in thermodynamics broadens the conventional entropy framework to address the non-extensive characteristics of BHs, especially those affected by quantum or exotic aspects. This study integrates Tsallis entropy with the energy emission processes and thermal fluctuations, linking particle motion to the thermodynamic characteristics of BHs and revealing how parameters such as κ and δ alter entropy and thermal radiation. Essentially, this comprehensive approach basically improves the comprehension of BH mechanics. The entropy equation quantifies the information

contained within a BH and its relationship to the horizon radius r_0.

7 Thermal fluctuations

This section examines the influence of thermal fluctuations on the thermodynamics of the newly proposed BH model. To investigate this influence, we use the Euclidean quantum gravity paradigm, in which the time axis is transposed into the complex plane. This approach allows us to define the partition function for the BH, as outlined in [107–112]. For a comprehensive elucidation, refer to reference [108], which encapsulates the streamlined methodology:

$$Z = \int Dg\,DA\,\exp(-I). \tag{42}$$

In this context, the integral runs across all fields that adhere to particular periodicity or boundary requirements, and the equation $I \to \iota\hat{I}$ reflects the field's Euclidean action. There is a connection between the references [113,114] and the statistical mechanical partition function:

$$Z = \int_0^\infty DE\Gamma(E)\exp(-\psi E), \tag{43}$$

where ψ represents the inverse of T. With a few mathematical calculations, one may find the density of states as follows:

$$\Gamma(E) = \frac{1}{2\pi i}\int_{\psi_0-i\infty}^{\psi_0+i\infty} d\psi e^{S(\psi)}. \tag{44}$$

Adding ψE to the natural logarithm of Z, one may obtain S_c. By removing thermal fluctuations, we find that the entropy is close to the equilibrium temperature ψ as $S = \delta\left(\pi r^2\right)^\kappa$. The entropy $S_c(\psi)$ is determined by [107] showing the thermal fluctuations are integrated as

$$S_c = S + \frac{1}{2}(\psi-\psi_0)\left(\frac{\partial^2 S(\psi)}{\partial\psi^2}\right)_{\psi=\psi_0}. \tag{45}$$

Therefore, the following formula can be utilized to describe the density:

$$\Gamma(E) = \frac{1}{2\pi i}\int_{\psi_0-i\infty}^{\psi_0+i\infty} d\psi e^{\frac{1}{2}(\psi-\psi_0)\left(\frac{\partial^2 S(\psi)}{\partial\psi^2}\right)_{\psi=\psi_0}}, \tag{46}$$

and

$$\Gamma(E) = \frac{e^S}{\sqrt{2\pi}}\left[\left(\frac{\partial^2 S(\psi)}{\partial\psi^2}\right)_{\psi=\psi_0}\right]^{\frac{1}{2}}. \tag{47}$$

It is possible to express the corrected entropy equation using the relation

$$S_c = S - \frac{1}{2}\ln\left[\left(\frac{\partial^2 S(\psi)}{\partial\psi^2}\right)_{\psi=\psi_0}\right]^{\frac{1}{2}}. \tag{48}$$

Equating the square of the energy fluctuation with the second derivative of entropy yields the result. Using the relationship between conformal field theory and the small degrees of freedom of a BH can simplify this expression [115]. The entropy, $S = m_1\psi^{n_1} + m_2\psi^{-n_2}$, is a result of the positive constants m_1, m_2, n_1, and n_2 [116].

The maximum entropy is achieved at $\psi_0 = \left(\frac{mn_2}{m_1n_1}\right)^{\frac{1}{n_1+n_2}} = T_H^{-1}$, where T represents the thermodynamic temperature as defined in Eq. (40). Extending the entropy in the vicinity of this peak results in the findings presented in [117,118]:

$$\left(\frac{\partial^2 S(\psi)}{\partial\psi^2}\right)_{\psi=\psi_0} = S\psi_0^{-2}. \tag{49}$$

A modified formulation of entropy, derived by omitting higher-order corrections, is presented as follows:

$$S_c = S - \frac{1}{2}\ln ST_H^2. \tag{50}$$

Since BHs are known to have quantum fluctuations, several questions about thermal fluctuations in BH thermodynamics have arisen. When the BH is small and exhibits a high temperature, the variations are noticeable. Quantum fluctuations might not matter for larger BHs. These structures with high temperatures are the most susceptible to thermal variations. When a BH shrinks in size, its temperature rises in tandem. As a result, these adjustment parameters are primarily relevant to extremely tiny BHs with high temperatures [107]. Then, by leaving out the correction elements of higher order, we can obtain the universal entropy formula:

$$S_c = S - \gamma\ln ST_H^2, \tag{51}$$

where γ is a parameter that regulates the intensity of the logarithmic correction resulting from thermal fluctuations and quantum phenomena, especially for small BHs. We define γ as a fixed parameter that includes the logarithmic correction terms related to thermal fluctuations. Setting γ to zero produces the entropy expression devoid of correction terms. As previously stated, for large BHs that exhibit very low temperatures, we consider $\gamma \to 0$, while for small BHs with elevated temperatures, we consider $\gamma \to 1$. By employing Eqs. (40) and (51), the corrected entropy formula can be derived:

$$S_c = \delta\pi^{\kappa}\left(r_0^2\right)^{\kappa} - \gamma \log\left(\frac{\delta\pi^{\kappa-2}\left(r_0^2\right)^{\kappa} e^{-\frac{2r_0}{\alpha M}}\left(2\alpha^3M^3\left(e^{\frac{r_0}{\alpha M}}-1\right)-2\alpha^2M^2r_0-\alpha Mr_0^2-r_0^3\right)^2}{16\alpha^6M^4r_0^4}\right). \tag{52}$$

We include thermal fluctuation-induced entropy modifications in our study, which are especially important for small BHs when quantum effects become important. The traditional Bekenstein–Hawking entropy is supplemented with logarithmic terms to introduce these corrections. This correction reflects the underlying quantum gravitational degrees of freedom and is a result of statistical fluctuations near thermal equilibrium in the canonical ensemble. The behavior of entropy with these corrections shows that, in the low-BH mass or temperature regime, the logarithmic term takes front stage, suppressing divergent behavior close to critical points. In addition to enhancing the system's thermodynamic stability, these adjustments suggest minor adjustments to the BH's geometry, which may have an impact on observable parameters. The corrected entropy S_C against r_0 is plotted for different values of the BH parameter α, the entropy parameters κ, δ, and the correction parameter γ for large BH ($\gamma = 0$), and for small BHs ($0 < \gamma \leq 1$) $\gamma = 0.3,\ 0.7,$ and 1.0. Here, Fig. 12 predicts that the corrected entropy increases uniformly throughout the range of r_0 for all the parameters mentioned.

Tsallis entropy provides a unique perspective on BH thermodynamics, differing from conventional entropy definitions such as the Bekenstein–Hawking entropy. The Bekenstein–Hawking entropy, expressed as $S_{BH} = \frac{A}{4G}$ (where A denotes the size of the event horizon), presupposes an extensive system in which entropy correlates with the BH surface area. However, this definition of entropy fails to incorporate quantum corrections or non-equilibrium effects, which are essential for more intricate BH models, such as those involving quantum gravity or exotic matter (e.g., hairy BHs). Conversely, the Tsallis entropy is a non-extensive entropy that incorporates the parameter κ, which addresses microscopic correlations and quantum effects, enabling it to represent the non-equilibrium characteristics of BHs. Tsallis entropy is particularly advantageous for characterizing BHs influenced by quantum fluctuations or exotic materials when the premise of extensiveness is invalid. Essentially, it offers a broader framework for comprehending BH thermodynamics, which includes modifications to the conventional entropy–area relationship. Moreover, thermal fluctuations, required for understanding the stability and thermodynamics of BHs, are included through Tsallis entropy.

The incorporation of thermal fluctuations alters the entropy, offering a more refined comprehension of the BH thermodynamics. One can specifically note that the parameter γ indicates the influence of these fluctuations on the total entropy, providing insights into the system's non-equilibrium behavior. Compared to other entropy definitions, Tsallis entropy provides a more precise characterization of BHs in non-extensive systems, integrating quantum and thermal phenomena that traditional entropy formulations, such as Bekenstein–Hawking entropy, fail to account for. The integration of Tsallis entropy with thermal fluctuation analysis results in a more comprehensive and dynamic model of BH thermodynamics, providing enhanced insight into their behavior under diverse physical conditions, including those affected by quantum and exotic matter.

8 Emission energy

Quantum fluctuations in BHs lead to ongoing particle creation and annihilation on a significant scale just outside the event horizon. The tunneling process [119–123] causes positively charged particles to be attracted to the core of the BH, which aids in the emission of Hawking radiation and ultimately contributes to the BH's evaporation over a finite period. The rate of evaporation is directly proportional to the rate of energy emission. The high-energy reception cross-section closely approximates the shadow of a BH for a distant observer. This cross-section demonstrates oscillations about a fixed, constrained value, σ_{lim}, which is associated with the radius of the BH [124–126]:

$$\sigma_{lim} \approx \pi r_0^2. \tag{53}$$

In this context, r_0 denotes the radius of the BH event horizon. The formula for the energy emission rate of a BH is provided as follows [125,126]:

$$\frac{\mathrm{d}^2\varepsilon}{\mathrm{d}\omega\mathrm{d}t} = \frac{2\pi^2\sigma_{lim}}{e^{\frac{\omega}{T_H}}-1}\omega^3. \tag{54}$$

The temperature is defined as $T_H = \frac{1}{4\pi}\frac{\partial f(r)}{\partial r}$. By replacing the horizon radius r_0, temperature T_H, and cross-section σ_{lim} into Eq. (54), one can derive the expression for the emission energy process:

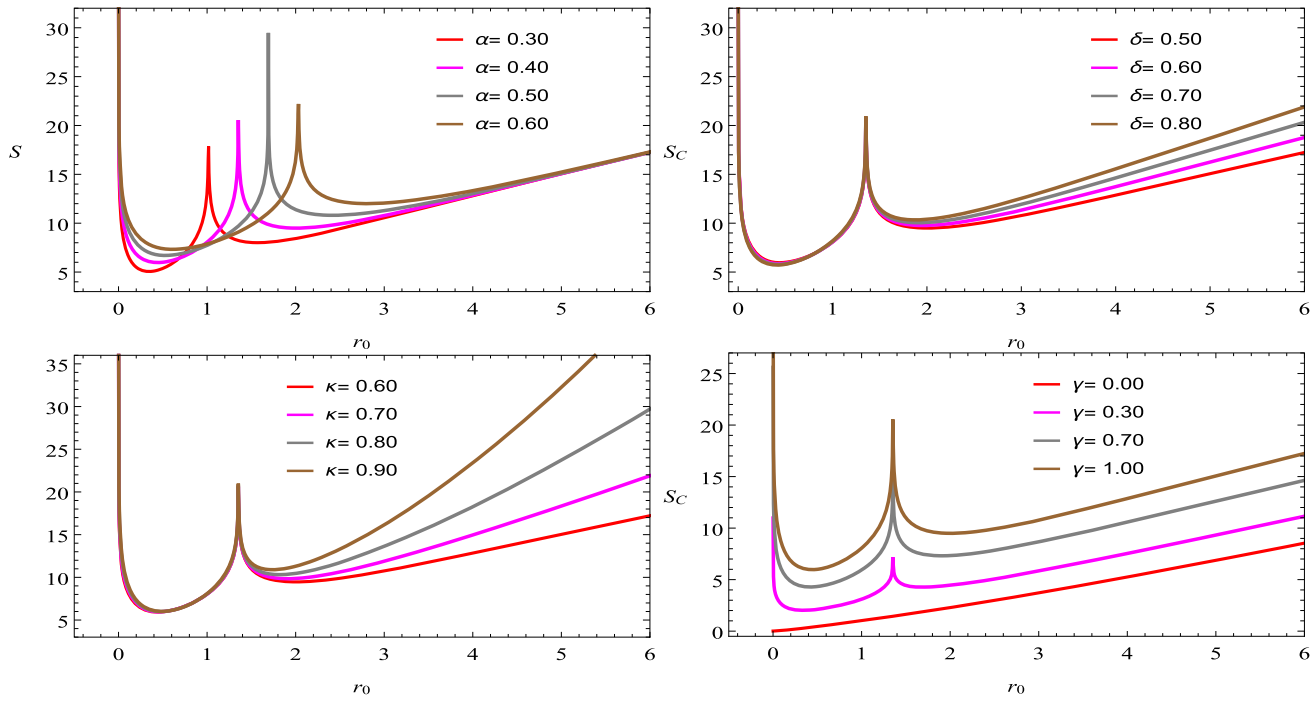

Fig. 12 Corrected entropy S_C along horizon radius r_0 to show the effect of thermal fluctuations by fixing $M = 1,\ \alpha = -0.5$

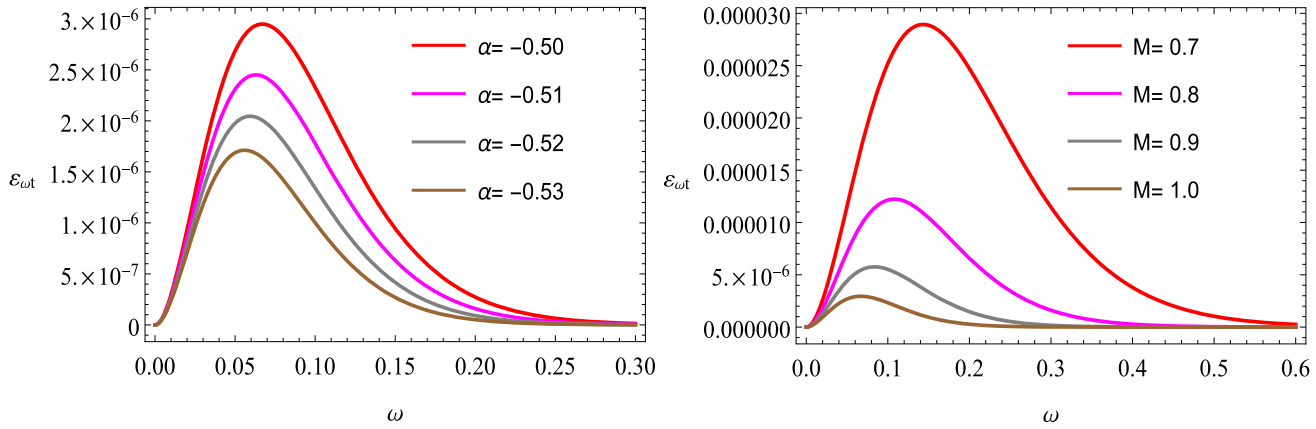

Fig. 13 Emission energy along ω by fixing $M = 1,\ \kappa = 0.6,\ \delta = 0.5,\ \alpha = 0.4$ and $\gamma = 1$

$$\frac{\mathrm{d}^2\varepsilon}{\mathrm{d}\omega \mathrm{d}t} = \left(2\pi^3 r_0^2\right)\omega^3\left[e^{2r_0^2\omega\left[\frac{e^{-\frac{r_0}{\alpha M}}\left(2\alpha^3M^3\left(e^{\frac{r_0}{\alpha M}}-1\right)-2\alpha^2M^2r_0-\alpha Mr_0^2-r_0^3\right)}{4\pi\alpha^3M^2r_0^2}\right]^{-1}} - 1\right]^{-1}. \tag{55}$$

The energy emission rate, determined by the modified entropy and Hawking temperature, signifies the influence of quantum and thermal fluctuations on black hole radiation. The incorporation of logarithmic adjustments results in a decreased Hawking temperature, subsequently minimizing the energy emission rate.

This indicates a decreased evaporation process of black holes, hence improving thermodynamic stability, especially for small BHs. The reduced emission is crucial for theoretical models of primordial BHs, which are potential sources of observable signatures in high-energy astrophysical contexts. We can obtain complete information on the energy emission phenomenon of the BH from Fig. 13. It is obvious from the

figure that $\varepsilon_{\omega t}$ decreases with increase in parameters α and M.

9 Conclusions

We have explored the complex interaction between BH properties and gravitational effects by studying the behavior of test particles in the spacetime of a spherically symmetric, non-rotating hairy regular BH. The hairy parameter α and the mass M affect the motion and physical properties of the system by including these factors together.

We have determined analytical formulas for the energy and angular momentum of test particles as functions of M and α by analyzing the stability of circular orbits within the effective potential framework. Insights into deviations from the Schwarzschild geometry have been further enhanced by the results, which demonstrated a clear dependence of these variables on the hairy parameter. Important changes caused by α were found in the effective forces on the particles and the position of the ISCOs, highlighting the role of these factors in controlling the motion of the particles.

We were able to see particle trajectories and investigate their epicyclic oscillations close to the equatorial plane by numerically integrating the equations of motion. Additional evidence of the effect of α on these oscillatory modes was given by analytical derivations of the radial, vertical, and orbital frequencies. The frequency of periastron precession was also calculated and displayed unique characteristics in contrast to the classical Schwarzschild scenario. One possible way to tell hairy regular BHs apart from their non-hairy relatives is by observing their unique characteristics.

We also studied thermal characteristics, going beyond particle dynamics, by studying thermal fluctuations and the energy emission process with Tsallis entropy. In addition to changing the dynamical aspects, our results show that the parameter α, coupled with the Tsallis entropy parameters δ, κ and the correction parameter γ, greatly affect the thermodynamic properties of BHs.

All the physics of particle motion and thermal processes around a hairy regular BH are explained in this paper. The findings highlight the significant impact of the BH parameters on the dynamics and observable characteristics, suggesting possible ways to investigate these spacetimes using astrophysical data and gravity experiments.

Our analysis bridges the gap between classical Schwarzschild BHs and more generalized models, enriching the theoretical framework for understanding gravitational systems and providing valuable insights for future observational endeavors involving BH environments.

The results of this study have important theoretical and practical implications for the future of this field of study. A possible observational signature could be the differential impacts of the hairy parameter α on orbital stability, ISCOs radius, precession frequencies, and thermal properties, especially in data from X-ray binaries, accretion discs, and gravitational wave sources. Potential tools for constraining α and testing this BH model include the EHT and future space-based detectors. We could learn more about spacetime if we could draw links between α and quantum gravitational corrections, and we could compare rotating spacetimes with Kerr BHs and frame-dragging effects if we extended the analysis to such spaces. Hairy BHs in binary systems can be detected using the derived frequencies, which can also improve the gravitational wave templates. In addition, the ways in which α affects the BH shadows and plasma dynamics point to potential avenues for investigating new astrophysical phenomena. BH thermodynamics, shadow imaging, and observational astrophysics are all improved in this work, which also provides a foundation for evaluating modified gravity theories.

As a final comment, our current analysis has results similar to the Schwarzschild model under a specific constraint (i.e., $\alpha \to 0$). However, as a future project, we would like to pursue the Kerr rotating version of the considered BH solution, which can provide us with a proper comparative platform for the Kerr case. For other modified theories of gravity, of course, our current analysis can be implemented along with additional numerical simulations and astrophysical observations.

Acknowledgements The author SKM is grateful for the continued support and encouragement from the administration of the University of Nizwa. SR would like to express his gratitude for the Visiting Research Associateship Programme at the Inter-University Centre for Astronomy and Astrophysics (IUCAA) in Pune, India, and also for the facilities at ICARD, GLA University, Mathura.

Data Availability Statement This manuscript has no associated data. [Authors' comment: Data sharing not applicable to this article as no datasets were generated or analysed during the current study. The necessary calculations and graphical discussion are already available in the manuscript.]

Code Availability Statement This manuscript has no associated code/software. [Authors' comment: This is a theoretical work and no new code/software has been generated. The numerical computation has been performed by using mathematica and python.]

Funded by SCOAP[3].

References

1. K. Akiyama et al., Astrophys. J. **875**, L1 (2019)
2. K. Akiyama et al., Astrophys. J. Lett. **875**, L2 (2019)
3. Q. Gan, P. Wang, W. Houwen, H. Yang, Phys. Rev. D **104**, 044049 (2021)
4. L. Ru-Sen et al., Astrophys. J. **859**, 60 (2018)
5. K. Akiyama et al., Astrophys. J. Lett. **930**, L14 (2022)
6. A.A. Grigorian, J. Dexter, Mon. Not. R. Astron. Soc. **530**, 1563 (2024)
7. J. Homan et al., Astrophys. J. **586**, 1262 (2003)
8. J. Rayimbaev, B. Ahmedov, A.H. Bokhari, Int. J. Mod. Phys. D **31**, 2240004 (2022)
9. M. Qi, J. Rayimbaev, B. Ahmedov, Eur. Phys. J. C **83**, 730 (2023)
10. L. Rezzolla, O. Zanotti, *Relativistic Hydrodynamics* (Oxford University Press, Oxford, 2013)
11. L. Rezzolla, S. Yoshida, T.J. Maccarone, O. Zanotti, Mon. Not. R. Astron. Soc. **344**, L37 (2003)
12. L. Amarilla, E.F. Eiroa, G. Giribet, Phys. Rev. D **81**, 124045 (2010)
13. Z. Stuchlík, A. Kotrlova, G. Torok, Astron. Astrophys. **525**, A82 (2011)
14. G. Torok, A. Kotrlova, E. Sramkova, Z. Stuchlík, Astron. Astrophys. **531**, A59 (2011)
15. Z. Stuchlík, A. Kotrlova, G. Torok, Astron. Astrophys. **552**, A10 (2013)
16. X. Jiang, P. Wang, H. Yang, H. Wu, Eur. Phys. J. C **81**, 1043 (2021)
17. G. Mustafa, I. Hussain, W.M. Liu, Chin. J. Phys. **80**, 148 (2022)
18. Y. Liu, G. Mustafa, S.K. Maurya, F. Javed, Eur. Phys. J. C **83**, 584 (2023)
19. A. Ingram, S. Motta, New Astron. Rev. **85**, 101524 (2019)
20. M. Kološ, M. Shahzadi, Z. Stuchlík, Eur. Phys. J. C **80**, 133 (2020)
21. M. Shahzadi, M. Kološ, Z. Stuchlík, Y. Habib, Eur. Phys. J. C **81**, 1067 (2021)
22. M. Shahzadi, M. Kološ, Z. Stuchlík, Y. Habib, Eur. Phys. J. C **82**, 407 (2022)
23. M. Kološ, M. Shahzadi, A. Tursunov, Eur. Phys. J. C **83**, 323 (2023)
24. M. Shahzadi, M. Kološ, R. Saleem, Y. Habib, A. Eduarte-Rojas, Phys. Rev. D **108**, 103006 (2023)
25. T. Naseer, Phys. Dark Univ. **46**, 101663 (2024)
26. A. Caliskan et al., J. High Energy Astrophys. **44**, 99 (2024)
27. B. Rasheed, A. Ditta, T. Naseer, F. Javed, G. Mustafa, Int. J. Geom. Methods Mod. Phys. (2024). https://doi.org/10.1142/S021988782450302X
28. G. Murtaza et al., J. High Energy Astrophys. **44**, 279 (2024)
29. G. Mustafa et al., Phys. Dark Univ. **47**, 101753 (2025)
30. S.K. Maurya et al., Phys. Dark Univ. **47**, 101806 (2025)
31. G. Mustafa et al., Phys. Dark Univ. **47**, 101825 (2025)
32. G. Mustafa et al., Phys. Dark Universe **46**, 101825 (2025)
33. T. Naseer, Int. J. Geom. Methods Mod. Phys. 2550143 (2025)
34. G. Mustafa et al., Nucl. Phys. B **1012**, 116812 (2025)
35. G. Mustafa et al., Phys. Dark Univ. **46**, 101644 (2024)
36. Y. Liu et al., Phys. Dark Univ. **42**, 101311 (2023)
37. Y. Liu et al., Eur. Phys. J. C **83**, 584 (2023)
38. R. Bousso, S.W. Hawking, Phys. Rev. D **54**, 6312 (1996)
39. G.T. Horowitz, A.R. Steif, Phys. Rev. D **42**, 1950 (1990)
40. D. Piriz, M. Roy, J. Wudka, Phys. Rev. D **54**, 1587 (1996)
41. Y.N. Obukhov, A.J. Silenko, O.V. Teryaev, Phys. Rev. D **84**, 024025 (2011)
42. O.Y. Tsupko, G.S. Bisnovatyi-Kogan, Gravit. Cosmol. **20**, 220 (2014)
43. A. Chatelain, M.C. Volpe, Phys. Lett. B **801**, 135150 (2020)
44. T.D. Le, Chin. J. Phys. **73**, 147 (2021)
45. G. Mustafa et al., Chin. Phys. C **46**, 125107 (2022)
46. S.L. Adler, R.B. Pearson, Phys. Rev. D **18**, 2798 (1978)
47. A. Övgün, I. Sakalli, J. Saavedra, C. Leiva, Mod. Phys. Lett. A **35**, 2050163 (2020)
48. M. Lyutikov, J.C. McKinney, Phys. Rev. D **84**, 084019 (2011)
49. J.C. Bustillo, P.D. Lasky, E. Thrane, Phys. Rev. D **103**, 024041 (2021)
50. P. Bizon, Phys. Rev. Lett. **64**, 2844 (1990)
51. S. Droz, M. Heusler, N. Straumann, Phys. Lett. B **268**, 371 (1991)
52. B.R. Greene, S.D. Mathur, C.M. O'neill, Phys. Rev. D **47**, 2242 (1993)
53. N.E. Mavromatos, E. Winstanley, Phys. Rev. D **53**, 3190 (1996)
54. M.S. Volkov, D.V. Galt'sov, Phys. Rep. **319**, 1 (1999)
55. J. Levin, G. Perez-Giz, Phys. Rev. D **77**, 103005 (2008)
56. M. Grould, F.H. Vincent, T. Paumard, G. Perrin, Astron. Astrophys. **608**, A60 (2017)
57. M. De Laurentis, I. De Martino, R. Lazkoz, Phys. Rev. D **97**, 104068 (2018)
58. R.P. Kerr, Phys. Rev. Lett. **11**, 237 (1963)
59. R. Penrose, *Gravitational Collapse: The Role of General Relativity*, pp. 252–276 (1969)
60. J. Levin, G. Perez-Giz, Phys. Rev. D **79**, 124013 (2009)
61. G. Perez-Giz, J. Levin, Phys. Rev. D **79**, 124014 (2009)
62. R. Grossman, J. Levin, G. Perez-Giz, Phys. Rev. D **85**, 023012 (2012)
63. Y.K. Lim, Z.C. Yeo, Phys. Rev. D **109**, 024037 (2024)
64. V. Misra, J. Levin, Phys. Rev. D **82**, 083001 (2010)
65. G.Z. Babar, A.Z. Babar, Y.K. Lim, Phys. Rev. D **96**, 084052 (2017)
66. Z.Y. Tu, T. Zhu, A. Wang, Phys. Rev. D **108**, 024035 (2023)
67. J. Healy, J. Levin, D. Shoemaker, Phys. Rev. Lett. **103**, 131101 (2009)
68. H.Y. Lin, X.M. Deng, Phys. Dark Univ. **31**, 100745 (2021)
69. Y. Feng et al., Phys. Scr. **99**, 085034 (2024)
70. T. Naseer, J.L. Said, Eur. Phys. J. C **84**, 808 (2024)
71. E. Demir et al., Chin. J. Phys. **91**, 299–315 (2024)
72. B. Siza et al., Eur. Phys. J. C **84**, 1203 (2024)
73. T. Naseer, M. Sharif, M. Faiza, B. Dayanandan, Eur. Phys. J. C **84**, 1187 (2024)
74. Y. Feng et al., Chin. J. Phys. **90**, 372–386 (2024)
75. T. Naseer, M. Sharif, F. Chand, Phys. Dark Univ. **47**, 101783 (2025)
76. T. Naseer, Astropart. Phys. **166**, 103073 (2025)
77. Y. Feng et al., Eur. Phys. J. C **85**, 18 (2025)
78. T. Naseer, G. Mustafa, Ann. Phys. **473**, 169886 (2025)
79. G. Mustafa et al., Phys. Rev. D **101**(10), 104013 (2020)
80. R. Karmakar, U.D. Goswami, Eur. Phys. J. C **84**(9), 969 (2024)
81. M. Ilyas, D. Ahmad, Chin. J. Phys. **88**, 901–912 (2024)
82. W. Hu, I. Sawicki, Phys. Rev. D **76**, 064004 (2007)
83. T. Naseer, M. Sharif, Eur. Phys. J. C **84**, 554 (2024)
84. T. Naseer, M. Sharif, Phys. Dark Univ. **46**, 101595 (2024)
85. Y.-S. Song, W. Hu, I. Sawicki, Phys. Rev. D **75**, 044004 (2007)
86. V.I. Zhdanov, O.S. Stashko, Y.V. Shtanov, Phys. Rev. D **110**(2), 024056 (2024)
87. A. Errehymy, Phys. Dark Univ. **44**, 101438 (2024)
88. K.P. Das, U. Debnath, A. Ashraf, M. Khurana, Phys. Dark Univ. **43**, 101398 (2024)
89. M. Ilyas, D. Ahmad, Chin. J. Phys. **88**, 901–912 (2024)
90. A. Jaiswal, R. Kumar, S.K. Srivastava, M. Govender, Chin. J. Phys. **89**, 325–339 (2024)
91. S. Fakhry, Astrophys. J. **961**(1), 8 (2024)
92. B. Hazarika, P. Phukon, Prog. Theor. Exp. **2024**(4), 043E01 (2024)
93. S. Jumaniyozov et al., Eur. Phys. J. C **84**(9), 964 (2024)

94. E. Ghorani et al., Eur. Phys. J. C **84**(10), 1022 (2024)
95. E. Abdelghani et al., Eur. Phys. J. Plus **137**, 1311 (2022)
96. M. Astorino, Phys. Rev. D **88**, 104027 (2013)
97. R. Gervalle, M.S. Volkov, Phys. Rev. Lett. **133**, 171402 (2024)
98. L.G. Collodel, D.D. Doneva, S.S. Yazadjiev, Astrophys. J. **910**, 52 (2021)
99. H.Y. Lin, X.M. Deng, Eur. Phys. J. C **83**, 311 (2023)
100. M. Armano et al., Phys. Rev. Lett. **116**, 231101 (2016)
101. J. Luo et al., Class. Quantum Gravity **33**, 035010 (2016)
102. W.R. Hu, Y.L. Wu, Natl. Sci. Rev. **4**, 685 (2017)
103. L. Meng, Z. Xu, M. Tang, arXiv:2411.01858
104. W. Abramowicz, Astron. Astrophys. **404**, L21 (2003)
105. G. Török, M.A. Abramowicz, W. Kluźniak, Z. Stuchlík, Astron. Astrophys. **436**, 1 (2005)
106. C. Tsallis, L. Cirto, Eur. Phys. J. C **73**, 2487 (2013)
107. B. Pourhassan, M. Faizal, Europhys. Lett. **111**, 40006 (2015)
108. G.W. Gibbons, S.W. Hawking, J.M. Perry, Nucl. Phys. B **138**, 141 (1978)
109. J.B. Hartle, S.W. Hawking, Phys. Rev. D **13**, 2188 (1976)
110. R.F. Sobreiro, V. Otoya, Class. Quantum Gravity **24**, 4937 (2007)
111. L. Bonora, A.A. Bytsenko, Nucl. Phys. B **852**, 508 (2011)
112. Z. Akhtar, R. Babar, R. Ali, Ann. Phys. **448**, 169190 (2023)
113. G.W. Gibbons, S.W. Hawking, Phys. Rev. D **15**, 2752 (1977)
114. V. Iyer, R.M. Wald, Phys. Rev. D **52**, 4430 (1995)
115. T.R. Govindarajan, R.K. Kaul, V. Suneeta, Class. Quantum Gravity **18**, 2877 (2001)
116. S. Carlip, Class. Quantum Gravity **17**, 4175 (2000)
117. S. Das, P. Majumdar, R.K. Bhaduri, Class. Quantum Gravity **19**, 2355 (2002)
118. J. Sadeghi, B. Pourhassan, F. Rahimi, Can. J. Phys. **92**, 1638 (2014)
119. W. Javed, R. Ali, R. Babar, A. Övgün, Eur. Phys. J. Plus **134**, 511 (2019)
120. A. Övgün, W. Javed, R. Ali, Adv. High Energy Phys. **2018**, 3131620 (2018)
121. W. Javed, G. Abbas, R. Ali, Eur. Phys. J. C **77**, 296 (2017)
122. W. Javed, R. Ali, G. Abbas, Can. J. Phys. **97**, 176 (2019)
123. W. Javed, R. Ali, R. Babar, A. Övgün, Chin. Phys. C **44**, 015104 (2020)
124. A. Ditta, X. Tiecheng, G. Mustafa, M. Yasir, F. Atamurotov, Eur. Phys. J. C **82**, 756 (2022)
125. A. Ditta, X. Tiecheng, R. Ali, F. Atamurotov, A. Mahmood, A.S. Mumtaz, Ann. Phys. **453**, 169326 (2023)
126. A. Ditta, X. Tiecheng, R. Ali, G. Mustafa, Nucl. Phys. B **994**, 116287 (2023)